Received: 10 June 2019 | Revised: 10 January 2020 | Accepted: 13 January 2020

DOI: 10.1002/mrm.28197

FULL PAPER

Magnetic Resonance in Medicine

Improved susceptibility-weighted imaging for high contrast and resolution thalamic nuclei mapping at 7T

João Jorge[1,2] | Frédéric Gretsch[2] | Elena Najdenovska[1,3] | Constantin Tuleasca[4,5,6] | Marc Levivier[4,6] | Philippe Maeder[3] | Daniel Gallichan[7] | José P. Marques[8] | Meritxell Bach Cuadra[1,3,5]

[1]Medical Image Analysis Laboratory, Center for Biomedical Imaging (CIBM), University of Lausanne, Lausanne, Switzerland

[2]Laboratory for Functional and Metabolic Imaging, École Polytechnique Fédérale de Lausanne, Lausanne, Switzerland

[3]Department of Radiology, Centre Hospitalier Universitaire Vaudois, University of Lausanne, Lausanne, Switzerland

[4]Department of Clinical Neurosciences, Neurosurgery Service and Gamma Knife Center, Centre Hospitalier Universitaire Vaudois, Lausanne, Switzerland

[5]Signal Processing Laboratory (LTS5), École Polytechnique Fédérale de Lausanne, Lausanne, Switzerland

[6]Faculty of Biology and Medicine (FBM), University of Lausanne (UNIL), Lausanne, Switzerland

[7]Cardiff University Brain Research Imaging Centre, School of Engineering, Cardiff University, Cardiff, UK

[8]Donders Institute for Brain, Cognition and Behaviour, Radboud University, Nijmegen, The Netherlands

Correspondence
João Jorge, LIFMET-CIBM, Station 6, École Polytechnique Fédérale de Lausanne, CH-1015 Lausanne, Switzerland.
Email: joao.jorge@epfl.ch

Funding information
Schweizerischer Nationalfonds zur Förderung der Wissenschaftlichen Forschung, Grant/Award Number: 157040 and 205321_153564; Centre d'Imagerie BioMédicale, Grant/Award Number: Annual funding

Purpose: The thalamus is an important brain structure and neurosurgical target, but its constituting nuclei are challenging to image non-invasively. Recently, susceptibility-weighted imaging (SWI) at ultra-high field has shown promising capabilities for thalamic nuclei mapping. In this work, several methodological improvements were explored to enhance SWI quality and contrast, and specifically its ability for thalamic imaging.

Methods: High-resolution SWI was performed at 7T in healthy participants, and the following techniques were applied: (a) monitoring and retrospective correction of head motion and B_0 perturbations using integrated MR navigators, (b) segmentation and removal of venous vessels on the SWI data using vessel enhancement filtering, and (c) contrast enhancement by tuning the parameters of the SWI phase-magnitude combination. The resulting improvements were evaluated with quantitative metrics of image quality, and by comparison to anatomo-histological thalamic atlases.

Results: Even with sub-millimeter motion and natural breathing, motion and field correction produced clear improvements in both magnitude and phase data quality (76% and 41%, respectively). The improvements were stronger in cases of larger motion/field deviations, mitigating the dependence of image quality on subject performance. Optimizing the SWI phase-magnitude combination yielded substantial improvements in image contrast, particularly in the thalamus, well beyond previously reported SWI results. The atlas comparisons provided compelling evidence of anatomical correspondence between SWI features and several thalamic nuclei, for

example, the ventral intermediate nucleus. Vein detection performed favorably inside the thalamus, and vein removal further improved visualization.

Conclusion: Altogether, the proposed developments substantially improve high-resolution SWI, particularly for thalamic nuclei imaging.

KEYWORDS

field tracking, motion correction, susceptibility-weighted imaging, thalamic nuclei, vein segmentation

1 | INTRODUCTION

Magnetic susceptibility is a tissue property that is sensitive to composition and microstructure, and can be probed non-invasively with certain MRI modalities.[1,2] Crucially, the pursuit of increasingly higher magnetic field strengths (B_0) has brought key enhancements in signal-to-noise ratio and contrast to these modalities,[3,4] resulting in enhanced sensitivity, and offering the possibility of exploring higher spatial resolutions. Along this line, recent works at ultra-high field strengths of 7T, investigating sub-millimeter T_2^*-weighted magnitude and phase data, have shown exquisite mapping capabilities for various cortical and subcortical features.[5,6] Also among these modalities is susceptibility-weighted imaging (SWI), which combines T_2^*-weighted magnitude and phase information at long echo time. While originally developed primarily for venography,[7] taking advantage of the geometry and paramagnetic content of veins,[8] SWI was soon found valuable for numerous other applications, including the detection of trauma, stroke, cortical dysplasia and tumors.[9,10] At 7T, SWI has shown enhanced sensitivity in detecting multiple sclerosis lesions[11] and features of polymicrogyria in epilepsy,[12] for example. These reports suggest a potentially substantial impact of SWI at ultra-high field for clinical neuroimaging in the near future, particularly as the number of clinically certified 7T systems rapidly increases worldwide.

Notably, 7T SWI has also shown promising capabilities for imaging the thalamus.[13] This subcortical brain structure is organized in smaller nuclei with specialized functions, that play key roles in neuronal signal transmission and modulation,[14,15] and have been a strong focus of neuroscience research, as well as clinical interventions. For example, neuronal deficits in the anterior and mediodorsal nuclei, as well as the pulvinar (Pu), have been linked to psychotic disorders such as schizophrenia.[16] The ventral intermediate nucleus (Vim) is commonly targeted to treat essential tremor[17]; this intervention can be done non-invasively, by radiosurgery[18-21] or focused ultrasound,[22] but requires accurate non-invasive targeting. Unfortunately, conventional modalities such as T_1 and T_2-weighted imaging offer poor contrast in the thalamus, and diffusion tensor imaging cannot resolve some of its individual nuclei, such as the Vim.[23] Indirect mapping approaches relying on standard atlases can provide further differentiation, but cannot fully account for individual anatomical variability. Promisingly, recent work with 7T SWI at high resolution has found unprecedented contrast features within the thalamus, which appear to be in good correspondence with the expected anatomy of its nuclei.[13]

Despite the potential of high-resolution SWI at 7T, the technique currently presents important unsolved challenges that can compromise image quality and diagnostic value. First, the high spatial specificity afforded by sub-millimeter voxel resolutions can be easily compromised by head motion occurring throughout the periods of several minutes required for acquisition, even in compliant subjects.[24] Additionally, susceptibility-based contrasts (typically T_2^*-weighted) are particularly sensitive to perturbations in B_0 over time, which can arise due to breathing.[25] Altogether, motion and field-related artifacts can introduce substantial blurring, ghosting and ringing artifacts, signal loss, and inhomogeneities.[24,26,27] Numerous groups have proposed techniques to monitor and compensate for motion-related effects,[28] and in some cases for field perturbations as well.[25,29] Yet, most studies so far have only tested such corrections on relatively limited datasets, focusing primarily on image magnitude, not phase, and often in conditions of large intentional motion or deep breathing, for proof-of-concept purposes.

Second, SWI, as conventionally implemented in commercial MR systems, is optimized to image veins.[7,8] The diverse applications for which it was subsequently found valuable constitute empirical findings, and most likely remain suboptimal with regard to contrast. It is currently unknown whether modifications of the SWI phase-magnitude combination, in particular, could enhance its ability to image non-venous tissues such as the thalamus. Previous reports have found promising results for thalamic mapping using the conventional, venography-oriented SWI contrast, but to our knowledge none have proposed or explored potential dedicated improvements.[13,30] A main reason for this shortcoming could be the fact that, to our knowledge, the SWI combination parameters are typically fixed and cannot be modified by users directly on the console ("online"), requiring dedicated expertise in MRI data reconstruction to explore such modifications.

Third, the inherent high sensitivity to the presence of veins of conventional SWI can, by itself, pose a nuisance to visualization in non-vein-related applications, and to

processing tasks like thalamic nuclei segmentation.[31] The inclusion of effective vein detection and segmentation approaches could prove valuable to inform subsequent processing steps, or even to remove the presence of veins altogether.

The present work aims to address the above-described limitations, introducing novel improvements to conventional SWI for high-resolution imaging at 7T, with a particular focus on thalamic nuclei mapping. The work comprised three main modifications: (a) concurrent monitoring of head motion and B_0 perturbations using integrated MR navigators,[32-34] and retrospective correction of the acquired data; (b) segmentation of venous vessels on the SWI data using vessel enhancement filtering,[35] and suppression of the veins by interpolation[36]; and (c) enhancement of the SWI contrast by tuning the parameters of phase high-pass filtering and phase-magnitude combination.[7] These modifications were implemented and tested on a group of healthy human participants, at 7T. Post-acquisition, the improvements obtained with motion and field correction were evaluated with quantitative metrics of image quality; the improvements produced by vein removal and contrast enhancement were evaluated by direct comparison with the more conventional (venography-oriented) version, and the anatomical correspondence of the enhanced features was studied by comparison to anatomo-histological atlas information, in the thalamus.

2 | METHODS

This study was approved by the local ethics committee (CER-VD), and involved the participation of 12 healthy volunteers (69 ± 7 years old, 4 male/8 female), who provided written informed consent. The dataset was acquired as part of a larger study on essential tremor, belonging to an age-matched control sub-group. All participants were clinically healthy, and did not exhibit any brain anomalies in previous 3T MRI scans.

Data processing was mainly performed in Matlab (Mathworks, Natick MA) using routines developed in-house, combined with tools from the Berkeley Advanced Reconstruction Toolbox[37] and the FMRIB Software Library (FSL).[38]

2.1 | Data acquisition

The acquisitions were performed on a Magnetom 7T head scanner (Siemens Healthcare, Erlangen, Germany) equipped with a birdcage transmit/32-channel receive radiofrequency array (Nova Medical, Wilmington, MA, USA). The participants were asked to lie as still as possible during image acquisition, with their eyes closed; head padding was employed to minimize motion. Each participant underwent a high-resolution SWI acquisition, and a whole-brain T_1-weighted acquisition for registration and comparison purposes. The SWI scan consisted of a flow-compensated 3D-gradient echo (GRE) sequence with 0.375 × 0.375 × 1-mm resolution, 192 × 192 × 72-mm field-of-view, TR/TE = 41/20 ms, $\alpha = 12°$, 120 Hz/Px bandwidth, 2 × undersampling and 6/8-partial Fourier in the first phase-encoding direction, and a total acquisition time (TA) of approximately 11 minutes. The imaging slab was placed in an axial-oblique orientation centered at the thalamus. The T_1-weighted scan used a 3D MP2RAGE sequence[39] with 0.6-mm isotropic spatial resolution, 192 × 192 × 154-mm (whole-brain) field-of-view, TE/TI_1/TI_2/TR = 4.94/800/2700/6000 ms, $\alpha_1/\alpha_2 = 7°/5°$, 240 Hz/Px bandwidth, 3 × GRAPPA acceleration in the first phase-encoding direction and 6/8 partial Fourier in both phase-encoding directions, and a TA of approximately 10 minutes. The raw GRE data of the SWI acquisition were exported for offline reconstruction, while the T_1-weighted image was reconstructed on-scanner.

2.2 | Integrated MR-based navigators and artifact correction

The GRE (SWI) acquisition included integrated MR-based navigators to monitor head motion and B_0 perturbations occurring throughout the acquisition. These navigators included two elements: highly-undersampled 3D GRE images of the head fat signal, termed FatNavs,[32,33,40] and free induction decay-based navigators, or FIDNavs (see Supporting Information Figure S1, which is available online, for sequence diagram). The FatNavs were implemented in segmented fashion, with two k-space lines acquired after each k-space line acquisition of the GRE host sequence, at a nominal spatial resolution of 4 mm isotropic, and yielding a temporal resolution of 2.2 s. The FatNav readouts contained two echoes to enable field map estimation, as previously proposed,[33] acquired with TE_1/TE_2 = 1.17/4.17 ms. An FIDNav was acquired directly after each excitation pulse of the host sequence.[34] The FIDNav was measured in 0.2 ms, and the total duration for the FatNav module was 10.8 ms, leading to an effective TR of 41 ms for the host sequence, as mentioned above.

After acquisition, and before reconstruction of the complex images, the acquired k-space lines of the host GRE were corrected for motion and field-related artifacts. As proposed in previous work,[34] 10 time-varying parameters (6 to describe rigid-body head motion, 4 to describe 1st-order linear field perturbations) were estimated from the FatNavs and used to train a 1st-order model linking a representative FIDNav signal to the correction parameters. In detail, the representative FIDNav signal was defined as

the mean signal during the associated FatNav measurement. For the kth FatNav correction parameter vector p_k (of length 10), the associated representative FIDNav signal f_k is then a vector of length $2N_C+1$ (with N_c the number of receiver channels), containing the real and imaginary parts of the signal, as well as a constant term of 1, which allows for slight time reference offsets between the FatNav and FIDNav signals. The coefficients of the matrix C describing the 1st-order model were then found by direct matrix inversion of the following equation:

$$Cf_k = p_k \tag{1}$$

using all the FatNav-derived parameters (ie, the f_k for all the values of k) for the estimation. Details of a similar method can be found elsewhere.[41]

The estimated model C was then reapplied to the individual FIDNav signals, to obtain correction parameters at higher temporal resolution (approximately 24 Hz). The parameter timecourses were then smoothed using a Tukey filter with 0.5-Hz constant window, 1-Hz passband.[34] As shown in previous work,[33] both motion and magnetic field perturbations up to the 1st spatial order can be efficiently corrected using a phase correction for translation and 0th-order field component, followed by a non-uniform fast Fourier transform for rotation and 1st-order field component. This correction was applied to the host GRE sequence, individually for each receive channel.

2.3 | GRE image reconstruction

To obtain high-quality reconstructions of both magnitude and phase data, well separated from coil sensitivity contributions,[42] the ESPIRiT approach was employed to estimate the complex coil sensitivities,[43] and combined with block coil compression to obtain a virtual "body coil-like" channel,[42] as proposed in previous work.[44] These steps were performed on the calibration data of the GRE acquisition (512 × 64 × 72 matrix, 32 receive channels). A geometric coil compression step was applied beforehand (from 32 to 15 channels), to reduce computational costs.[45] After ESPIRiT estimation, the actual coil sensitivities were joined with the virtual "body coil" channel, which provided a singularity-free phase reference, and the full GRE data were thereby reconstructed using SENSE.[42,43] Subsequently, the phase data underwent Laplacian-based spatial unwrapping,[46] and background field removal using the Laplacian boundary value approach.[47] These preprocessing steps have previously been found to improve SWI quality,[48] and the additional computation time was not problematic for this offline processing.

2.4 | Evaluation of motion and field artifact correction effects

Seeking to quantitatively evaluate the impact of motion and field artifact corrections on image quality, a number of quality metrics were tested based on previous reports.[49,50] Among these, a modified version of the "normalized gradient squared" metric[49] exhibited the best trade-off between low variability across subjects and high sensitivity to artifact reductions, and was therefore selected for analysis. The metric was applied to the GRE data reconstructed with (a) no correction, (b) motion correction, and (c) motion and field correction. It was evaluated not only on the magnitude, but also, separately, on the phase images, given the importance of both for susceptibility-based contrasts in general, and SWI in particular.[2] The adopted metric can be referred to as "excess normalized gradient squared", S. Given a magnitude or phase image I, and a region of interest ROI, S was defined as:

$$S_{ROI} = \frac{E\left\{G\left(\vec{r}\right)^2\right\}_{ROI}}{E\left\{G\left(\vec{r}\right)\right\}_{ROI}^2} - C \tag{2}$$

$G\left(\vec{r}\right)$ denotes the norm of the image gradient of $I\left(\vec{r}\right)$, computed based on finite differences, at position $\vec{r}$; I was lightly smoothed beforehand [Gaussian smoothing, 1.1 mm full-width-at-half-maximum (FWHM)], to reduce the impact of random noise on the gradient computation. $E\{\cdot\}_{ROI}$ denotes the average over all voxels of ROI; two regions were considered: the whole brain, segmented from the magnitude image,[51] and the thalamus, given by an atlas mask co-registered from MNI space (see Section 2.7). C is a correction factor that centers the metric at 0, such that an input image of pure noise would yield $S = 0$, and a structured image will yield the "excess" relative to this pure noise case. C was estimated to be approximately 1.59 for magnitude images, and 1.33 for phase images.

To evaluate potential links between image quality and motion or field perturbations, each subject was also attributed a single measure reflecting the extent of head motion exhibited during acquisition, and another for the extent of field perturbations. First, head displacement at each timepoint was estimated as the norm of the displacement of each voxel in the brain relative to its position at the time of acquisition of the k-space center, averaged across all brain voxels. A single measure was then extracted as the root-mean-square (RMS) of the displacement across time. The field deviation at each timepoint was calculated as the absolute field shift relative to B_0 in each voxel, averaged across all brain voxels. A single measure was then extracted as the RMS of this field deviation across time.

2.5 | Vein segmentation and exclusion

Vein segmentation was performed using multiscale vessel enhancement filtering,[35] an image-based technique that uses 2nd-order (curvature) information to highlight vessel-like structures. Several variants of this approach have been successfully applied to MRI modalities,[52,53] including SWI.[54] In the present work, the technique was applied to the reconstructed SWI data tuned to the conventional contrast (see Section 2.6), which is optimal for vessel visualization.[8] Based on preliminary tests, the technique was found most effective when applied in 2D fashion, slice by slice (see Section 3.2 for details). The filter was set to cover a range of spatial scales of 0.4-1.2 mm, which was chosen based on the image resolution and the size of vessels typically found inside the thalamus.

Filter parameters $\beta = 0.5$ and $c = 5.0$ were determined empirically by direct visual inspection of the resulting vein maps, where we sought to optimize the compromise between false negatives and false positives in vein detection—an approach that was feasible since veins are visually well discernible in SWI data, and the subject group size was not prohibitively long. The resulting filter maps were thresholded at 0.4 (also determined by visual inspection) to create vein masks. The corresponding vein voxels were accordingly marked as "corrupted," and replaced by interpolation using neighboring voxel information (also termed "in-painting"), using the discrete cosine transform.[36]

2.6 | SWI combination and contrast enhancement

After GRE reconstruction (magnitude and phase data), SWI images were obtained following the originally proposed phase-magnitude combination[7]: (1) the phase image is spatially highpass-filtered; (2) a phase mask $f(\vec{r})$ is created from the filtered phase map $\varphi(\vec{r})$ following the expression:

$$f(\vec{r}) = \begin{cases} 1, & \varphi(\vec{r}) < 0 \\ (\pi - \varphi(\vec{r}))/\pi & \varphi(\vec{r}) \geq 0 \end{cases} \quad (3)$$

for each position $\vec{r}$ in the image; and (3) the magnitude image is multiplied by the phase mask a number of times m, thereby progressively reducing the intensity of voxels with positive φ.

Unlike the Hanning filter employed in the original approach,[55] the highpass filtering step was here based on Gaussian smoothing, that is, the original phase image was subtracted of a lowpass-filtered version of the same image obtained with Gaussian smoothing, with FWHM σ. This allowed a more direct interpretation of the range of spatial scales that were preserved and passed on to the phase mask f. Altogether, this framework allowed exploring multiple variations of the SWI contrast by varying both σ and m. Preliminary tests indicated that a combination of $\sigma = 4$ mm, $m = 4$ yielded the closest match to a more conventional SWI contrast, as produced by the vendor-supplied online reconstruction in our system (see Section 3.3).

2.7 | Image co-registration and atlas comparisons

To investigate the correspondence between SWI features and the expected thalamic anatomy, the processed images were compared with three histological atlases: (a) the Morel stereotactic atlas of the human thalamus[56]; (b) the Schaltenbrand atlas, based on detailed neuroanatomical information, including a delineation of the Vim[57]; and (c) BigBrain, a high-resolution image of a histological brain preparation, stained for the presence of cell bodies.[58] To allow direct comparisons, the individual subject data were registered to MNI space, using (1) the FLIRT tool of FSL[59] for linear registration between the SWI and T_1-weighted images of each subject, and (2) the FNIRT tool[38] for non-linear registration between the individual T_1-weighted images and the MNI T_1 template. The non-linear alignment between the T_1 and MNI images yielded displacement fields that were then applied to the SWI data, in combination with the estimated linear registration matrices. This non-linear step was found valuable to account for individual anatomical variability; nonetheless, its estimation relied exclusively on the T_1 (not SWI) data, thereby avoiding any potential comparison biases from "forced" local anatomical matching between the SWI and atlas features.

3 | RESULTS

3.1 | Motion and field artifact correction

Based on the navigator estimates, the acquired subjects exhibited head displacement RMS values of 0.12-0.41 mm, and B_0 field deviation RMS of 1.5-4.6 Hz, for the 11-minute SWI acquisition. Across time, both measurements were dominated by slow drift contributions, but also faster oscillations around 0.18-0.32 Hz (Supporting Information Figure S2). These oscillations were especially evident on the field perturbation timecourses.

The normalized gradient squared, serving as a metric of image quality, exhibited considerable variability across subjects, but showed nevertheless fairly consistent trends (Figure 1). These trends were approximated with robust linear fits across subjects, to ease their evaluation, although without a priori expectations of a linear behavior. Averaged across the brain, image quality tended to decrease with increasing head motion (displacement RMS) in both magnitude and

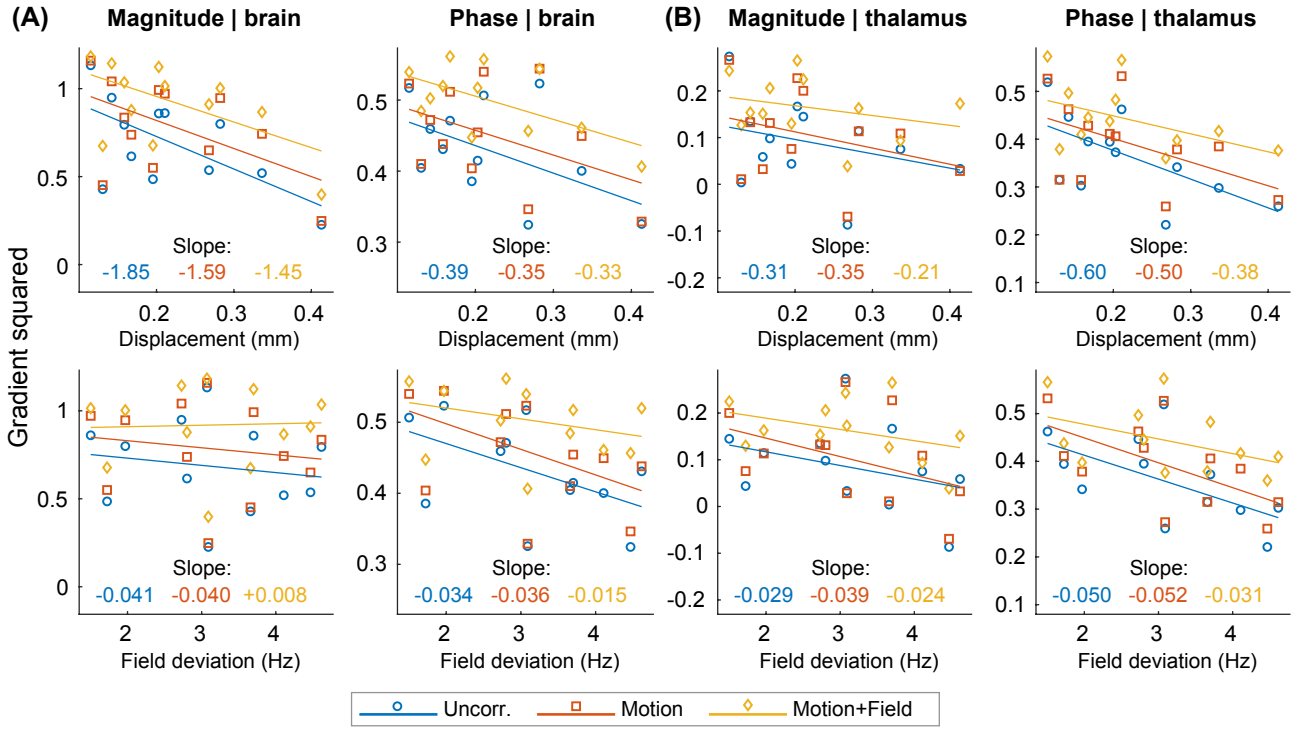

FIGURE 1 Variations in GRE image quality across subjects as a function of head motion (displacement RMS) or field fluctuations (field deviation RMS), before and after correcting for motion and field artifact contributions. Image quality is described based on the (excess) gradient squared metric, applied separately to the magnitude and phase data, voxel by voxel, and averaged across the whole brain (A) or the thalamus (B). Each dot corresponds to a specific subject, with a given correction approach; the straight lines correspond to robust linear fits to the subject data points for each of the correction approaches (obtained with Matlab function *robustfit*), and their slopes are provided below in the same respective color

phase data, especially before corrections (Figure 1A, upper). Correcting for motion, and further for motion and field artifacts, yielded consistently higher image quality in each subject, and tended to mitigate the overall decrease in quality with displacement RMS, as shown by the weaker slopes of their linear fits. A tendency for decreasing image quality with increasing field deviation RMS could also be observed (Figure 1A, lower), particularly in the phase data. Likewise, correcting for motion, and especially for motion and field artifacts, tended to mitigate this dependence. Overall, the trends observed for the whole brain were also reflected at the level of the thalamus (Figure 1B), although the effects on the magnitude data were less clear, with stronger variability across subjects, whereas the effects on the phase were more pronounced.

For further insights, the relative variation in gradient squared across the different correction steps (uncorrected, motion artifact-corrected, motion and field artifact-corrected) was also estimated. For the whole-brain ROI, the full correction resulted in substantial quality improvements of 4.4%-75.9% for the magnitude data and 4.3%-40.7% for the phase, across subjects. The previously observed concurrent dependences on head displacement and field deviation (Figure 1) motivated plotting these improvements as a function of both parameters (Figure 2). Overall, the quality improvements tended to be larger for the cases of larger head displacement and/or larger field deviation. Notably, the impact of motion correction was primarily dependent on the amount of head displacement (Figure 2, left), while the impact of field correction showed a dependence on both displacement and field deviations (Figure 2, center). These observations held for both magnitude and phase data, although the phase showed a more pronounced dependence on field perturbations than the magnitude.

Alongside their ROI-averaged effects, motion and field perturbations each created particular local artifacts that were directly visible in the GRE images. For instance, in datasets more affected by motion than field perturbations (Figure 3A; full slice in Supporting Information Figure S3A), the most evident artifacts in the magnitude were typically blurring and ringing of fine high-contrast features such as veins (Figure 3A, yellow circles; difference maps in Supporting Information Figure S4A). In the phase, veins were also affected, albeit by more intricate artifacts due to the complex dipolar geometry of venous phase features (Figure 3A, orange circles); blurring effects along the gray-white matter boundary could also be seen (red arrows). These artifacts were substantially reduced mainly by the motion correction step.

In datasets relatively more affected by field perturbations than motion (Figure 3B; full slice in Supporting Information Figure S3B; difference maps in Supporting Information Figure S4B), ringing and blurring effects could also be observed on the images (Figure 3B, orange

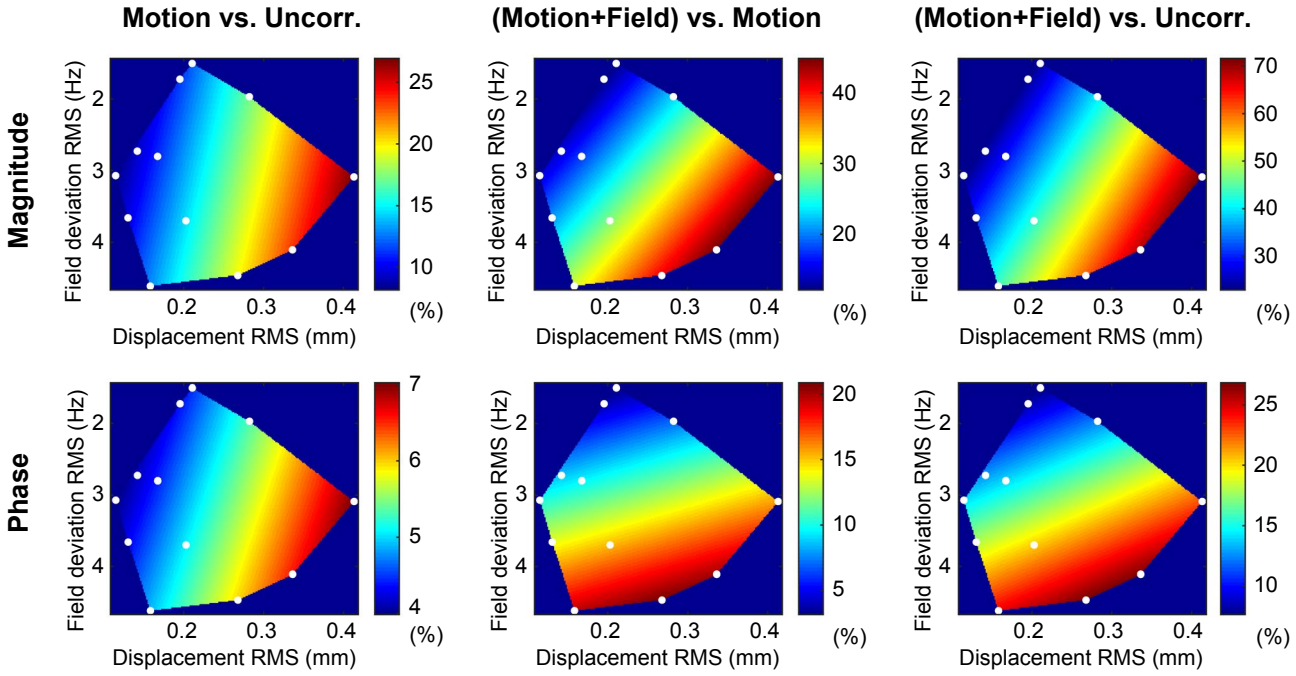

FIGURE 2 Variations in individual GRE image quality between the different artifact correction steps, as a function of head motion (displacement RMS) and field fluctuations (field deviation RMS), combined. The variations in image quality are described in terms of relative changes in the excess normalized gradient squared, applied separately to the magnitude and phase data, voxel by voxel, and then averaged across the whole brain. Each white dot corresponds to a specific subject; the 2D distributions were obtained as robust linear fits to those individual data points

and yellow circles); additionally, both large-scale and focal regions of abnormal hypo- and hyper-intensity could be observed (red arrows). In this case, the artifacts were not visibly reduced by the motion correction step, but only by field correction. The analysis of such "field-dominated" cases (ie, with relatively more important field deviations than motion) evinces the improvements yielded by field correction alone, since the motion contribution to the motion + field correction is close to negligible. Also of note, some subjects in the group exhibited no discernible artifacts whatsoever, typically consistent with lower estimated displacements and field deviations (Supporting Information Figure S5).

3.2 | Vein segmentation and exclusion

Based on visual inspection, the adopted vessel filtering approach was found considerably effective across the brain (Figure 4A, Supporting Information Figure S6). Preliminary tests showed that the 2D (slice by slice) implementation adopted for this work was more appropriate than a full 3D filter, most likely due to the strong anisotropy of the SWI voxel resolution (Supporting Information Figure S7). The filter scale range allowed the correct detection of most vessel calibers, except for the large sinuses and veins larger than the vein of Galen,[54] for example (Figure 4B, red arrows). On the low-end of the range, only a few of the smallest visually discernible veins were missed (Figure 4A, red arrows). These filter parameters were also found effective for the particular range of vessels that traversed the thalamus (Figure 4B). Based on the resulting vein masks, the interpolation procedure then yielded mostly vein-free thalamic images, while correctly preserving other hypo-intense regions of non-tubular geometry, and likely of anatomical relevance (Figure 4B, yellow arrows).

For a more comprehensive understanding of the presence of veins within the thalamus, the individual vein masks were brought to MNI space, and average vein densities were estimated for different thalamic sub-regions, based on the Morel atlas. On average, the thalamus as a whole exhibited a vein density of 4.7%, which then ranged between 0% and 21.6% across sub-regions. Higher densities were observed for more medial, relative to lateral nuclei (Figure 5A). A direct inspection of individual SWI data confirmed this observation (Figure 5B), showing that the medial thalamic regions were often perforated by superior thalamic (yellow arrows) and anterior thalamic veins (green), which drained to internal cerebral veins, in agreement with the expected anatomy.[54,60] In a few cases, small perforating veins (Figure 5B, red) could also be discerned in inferior-posterior areas, draining to basal veins; these possibly originated the slightly increased vein density observed for the Pu, although only seen on the right side (Figure 5A).

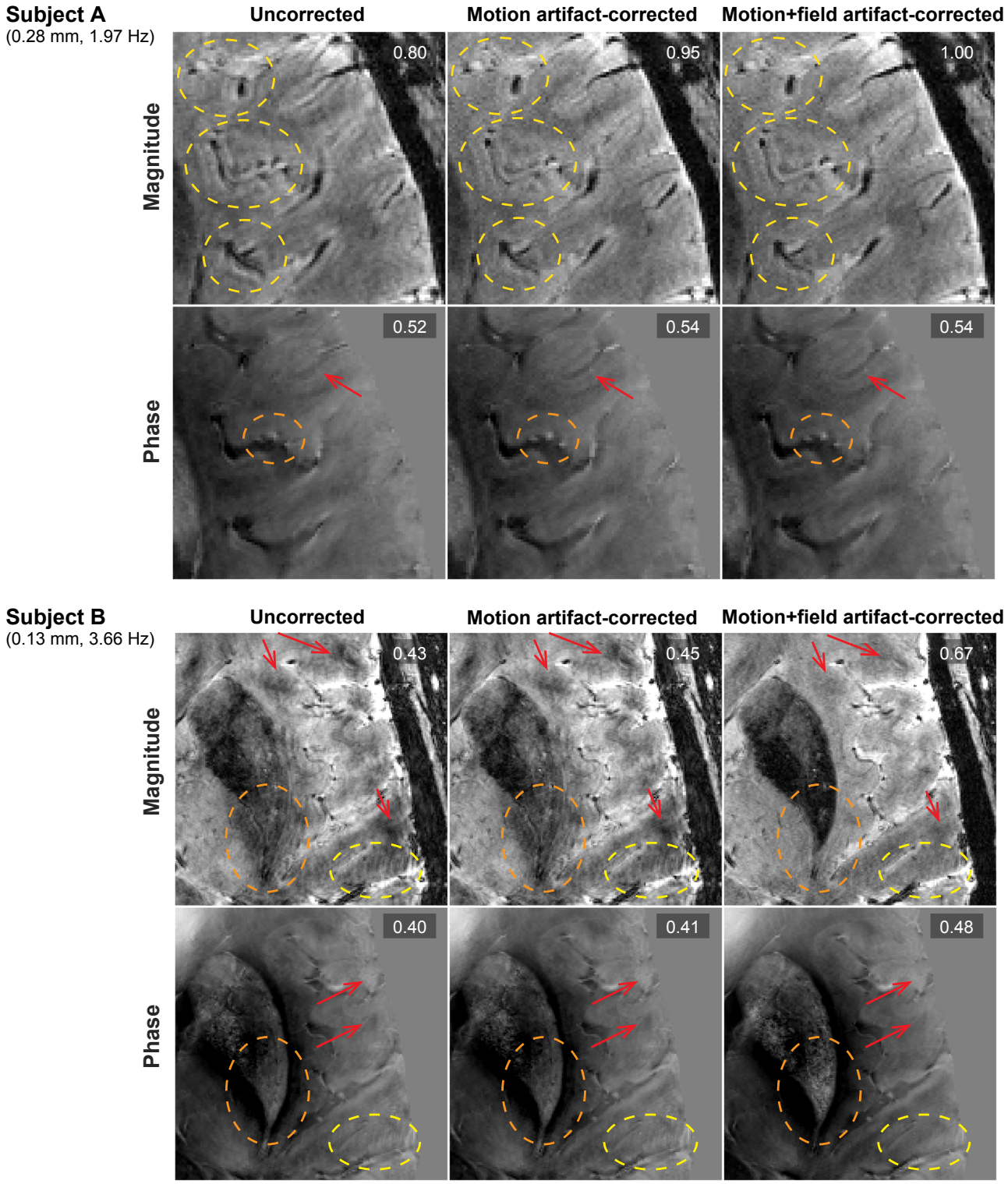

FIGURE 3 Local improvements in GRE magnitude and phase data achieved with motion and field artifact correction, in two example subjects. Subject A exhibited a relatively larger incidence of motion (0.28 mm displacement RMS) than field perturbations (1.97 Hz deviation RMS); subject B exhibited the opposite (0.13 mm displacement, 3.66 Hz deviation). The gradient squared estimates for each magnitude and phase image are indicated on the respective top right corner. The arrows and traced circles highlight regions that were particularly affected, and improved with correction; these artifacts included blurring, ringing, ghosting, and local hypo- and hyper-intensities

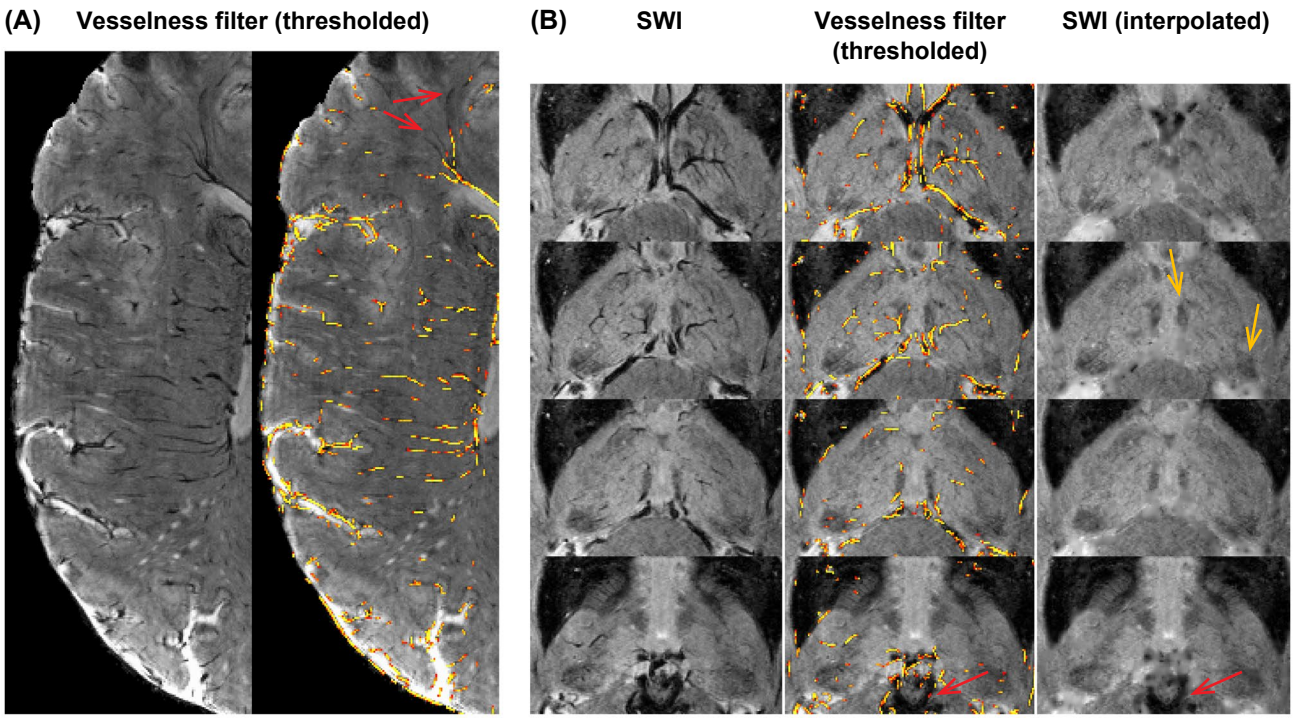

FIGURE 4 Vein detection and interpolation in the SWI data (conventional contrast) of an example subject. A, Vesselness filter output overlaid on the SWI data, thresholded with the same cutoff applied to create the vein masks. The red arrows indicate an example of very small-caliber veins that were missed by the filter. B, Example of the performance of vein interpolation in four slices of the thalamus, which exhibited both subtle as well as larger veins, crossing various thalamic nuclei. The red arrows indicate an example of large-caliber veins that were not detected by the filter; the yellow arrows indicate examples of hypo-intense regions of non-tubular geometry, and likely of anatomical relevance, which were correctly ignored by the filter

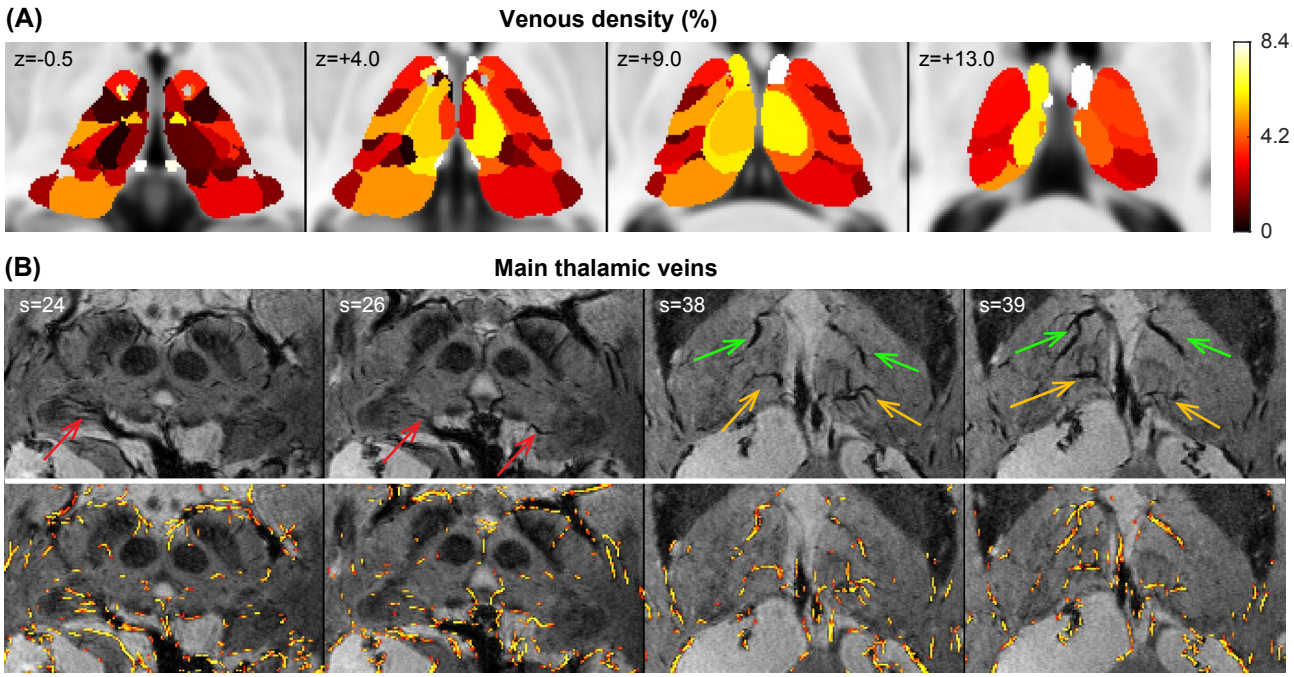

FIGURE 5 Distribution of veins in the thalamus based on the estimated vein masks. A, Venous density averaged within each thalamic region of the Morel atlas[56] and across subjects, in MNI space; the high-end of the color scale is adjusted to the 90th-percentile of densities, for clearer visualization. B, Examples of the main thalamic veins observed in individual SWI data, including the basal veins, with perforating vessels (red arrows), superior thalamic veins (yellow arrows), and anterior thalamic veins (green arrows). The lower row shows an overlay of the vesselness filter output over the same thalamic slices, thresholded with the same cutoff used to create the vein masks. The numbers in black (A) indicate the *z*-planes selected from MNI space, in mm; the numbers in white (B) indicate the slices selected from the native SWI slab

3.3 | SWI contrast enhancement

Variations in the phase highpass filtering FWHM σ, and the number of phase mask multiplications m, were both found to induce substantial changes in the resulting SWI contrast, namely in the thalamus (Figure 6). In particular, applying less restrictive filtering (larger σ) resulted in more extended, darker features; increasing the multiplication factor also enhanced their contrast relative to surrounding areas, eventually leading to signal saturation in regions like the Pu. As indicated in Section 2.6, a combination of $\sigma = 4$ mm, $m = 4$ (Figure 6, blue) yielded the closest match to a conventional SWI contrast (Supporting Information Figure S8). A higher-contrast combination of $\sigma = 7$ mm, $m = 10$ (Figure 6, green) displayed a favorable trade-off between enhancing contrast and avoiding saturation, and was thereby considered for further analyses.

To investigate the anatomical correspondence of SWI features to sub-regions of the thalamus, these data were compared to the T_1-weighted acquisitions and to reference information from the Morel atlas and BigBrain, warped to the native SWI space, to preserve its sharpness (Figure 7). Consistent with previous reports, the T_1-weighted modality exhibited poor contrast inside the thalamus. Conventional SWI exhibited more differentiated, although subtle, features. These features were then strengthened on the enhanced SWI contrast, clearly improving their visualization. It was also found that such improvements could not be achieved in conventional SWI by simply scaling the image contrast in visualization.

Regarding the anatomy, a comparison with the Morel atlas permitted several observations: at the posterior-inferior end, a relatively large hypo-intense region was well matched with the expected location of the Pu (Figure 7, $s = 17/25$); in superior axial cuts ($s = 30$), the observed features mainly showed a lateral vs. medial differentiation, which followed the organization of the atlas, distinguishing more lateral nuclei, including lateral posterior (LP), ventral posterolateral (VPL), ventral lateral (VL), and ventral anterior (VA), from the mediodorsal group (MD); in more intermediate cuts ($s = 25$), this lateral vs. medial organization was further differentiated by light-dark alternations, which appeared in agreement with the organization of the parafascicular (Pf) and central lateral (CL) nuclei more medially, then the centromedian (Ce), and more laterally the VPL (anterior and posterior), VL and ventromedial (VM) nuclei. Regarding cell body density (BigBrain), an identifiable correspondence to SWI could be observed for regions like the Pu and MD, while several other features detected by SWI were not differentiated by the cell body contrast. Overall, these observations were fairly robust across the subject group (eg, Supporting Information Figure S9); some other interesting observations included a visibly heterogeneous structure within the MD, showing a hypointense "arc shape" in medial-anterior (and possibly posterior) sub-regions, around a lighter lateral sub-region, which could be observed in both SWI and BigBrain for several subjects (eg, Supporting Information Figure S9A,B, top slice), but less clearly in others (eg, Figure 7). Of note, in the SWI

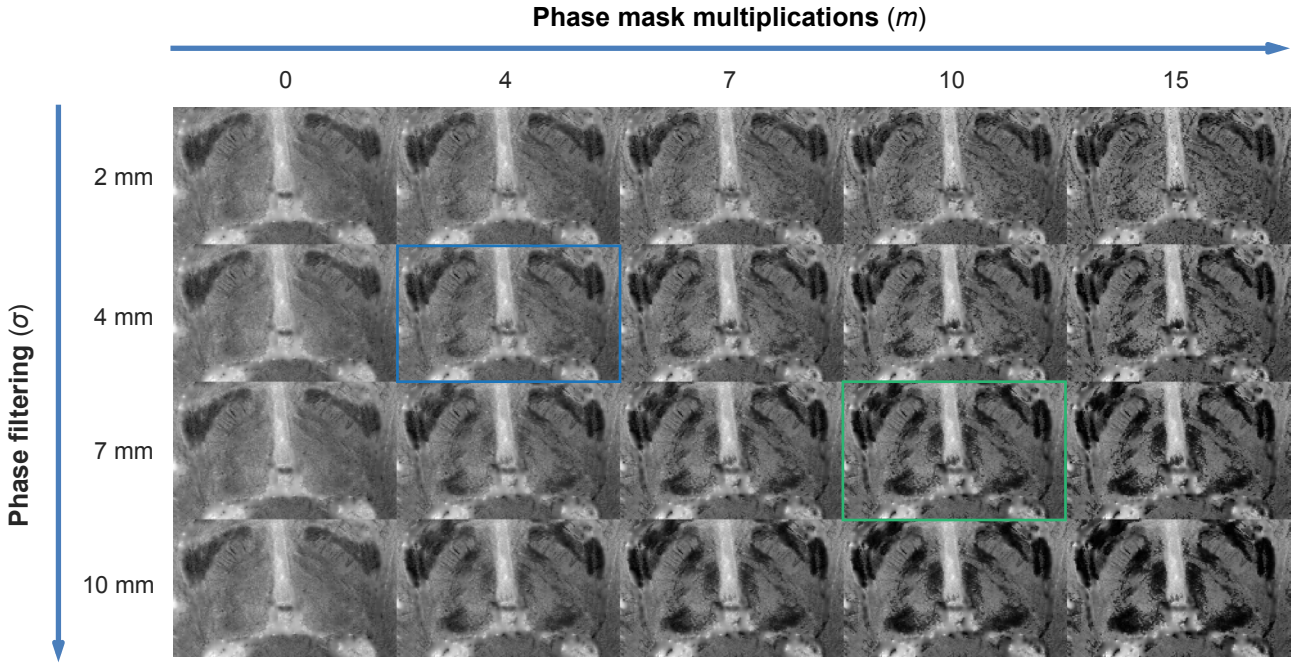

FIGURE 6 Variations of the SWI contrast obtained when increasing the FWHM σ of the Gaussian-based high-pass filtering of the phase data (top to bottom) and the number m of multiplications of the phase mask into the magnitude data (left to right). The case that most closely matches a conventional SWI contrast, as produced by the online reconstruction of our system, is indicated in blue ($\sigma = 4$ mm, $m = 4$). An enhanced case, which was empirically selected for further analysis, is indicated in green ($\sigma = 7$ mm, $m = 10$)

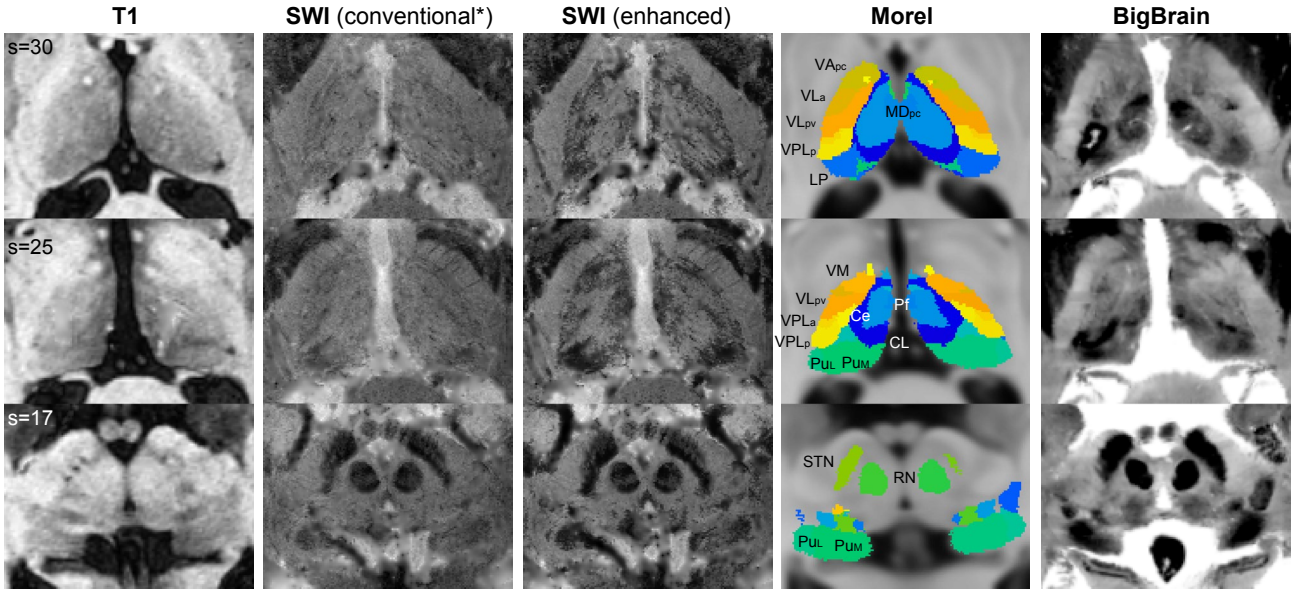

FIGURE 7 Image contrast in the thalamus of an example subject obtained with different imaging modalities, co-registered to the SWI native space: T_1-weighted contrast from the MP2RAGE acquisition (1st column); SWI with close-to-conventional contrast, that is, the closest output of our approach ($\sigma = 4$ mm, $m = 4$) to the scanner online reconstruction (2nd column; marked with a * to highlight its difference from the originally proposed approach[7]); and SWI with enhanced contrast ($\sigma = 7$ mm, $m = 10$; 3rd column). Reference information from the Morel atlas (4th column) and BigBrain (5th column) are shown for anatomical comparison; the colors of the Morel atlas are attributed randomly, simply to differentiate its sub-regions; the contrast in BigBrain is hypo-intense for regions of higher cell body density.[58] The Morel atlas labels indicate the ventral anterior (VA), ventral lateral (VL), ventral posterolateral (VPL), lateral posterior (LP), mediodorsal (MD), ventromedial (VM), pulvinar (Pu), centromedian (Ce), parafascicular (Pf), central lateral (CL), sub-thalamic (STN), and red (RN) nuclei. Three slices are shown, ascending through the thalamus from the bottom to the top row; the numbers on the top-left indicate the slices selected from the native SWI space

data, a certain degree of spatial continuity across slices could be observed between regions like the MD and the red nucleus (RN) below, and similarly for the VM and the sub-thalamic nucleus (STN), for example (Supporting Information Figure S10). While these pairs of regions showed clear differentiations in shape, excluding the possibility of some regions being simply an extension of the susceptibility effects produced by others, the geometries shown by the Morel atlas and BigBrain did suggest clearer spatial separations between these structures than those shown on SWI.

Further anatomical insights were pursued by bringing the enhanced SWI data to MNI space, for direct comparison to the Schaltenbrand atlas. At $z = 3.5$ mm, and consistent with the observations made in native space, SWI exhibited a rich distribution of hypo- and hyper-intense features (Figure 8). The most posterior hypo-intense area matched the atlas indication for the Pu, particularly for its lateral sub-regions (Figure 8, green); a medial region was well-matched to Pf (blue); laterally, two regions matched the ventro-caudalus (Vc, purple) and the ventro-odalis (Vo, red)/latero-polaris (Lpo, orange) group. Based on the distribution of these dark regions, a series of neighboring nuclei could then be indirectly located, such as Ce (Figure 8, pink) and the Vim nucleus (yellow). As in native space, the SWI features appeared to be anatomically richer than BigBrain's, and were overall fairly consistent across subjects (Figure 8).

4 | DISCUSSION

The present work builds on the promising brain imaging capabilities demonstrated by magnetic susceptibility-based contrasts at ultra-high field in recent years,[2,5] and explored a series of novel technical improvements for high-resolution SWI, with a particular focus on thalamic imaging.[13] These improvements included: (a) monitoring and compensation of head motion and B_0 field perturbations during SWI acquisition, to increase image quality; (b) segmentation and removal of venous vessels from the SWI data, to mitigate their confounding effects; and (c) modifications of the SWI contrast by tuning its phase-magnitude combination, for increased image contrast. To our knowledge, this is the first work employing these techniques for high-resolution SWI of the thalamic nuclei, and evaluating their benefits. The reported findings also extend to a wider scope of applications, namely regarding susceptibility-based contrasts in general.

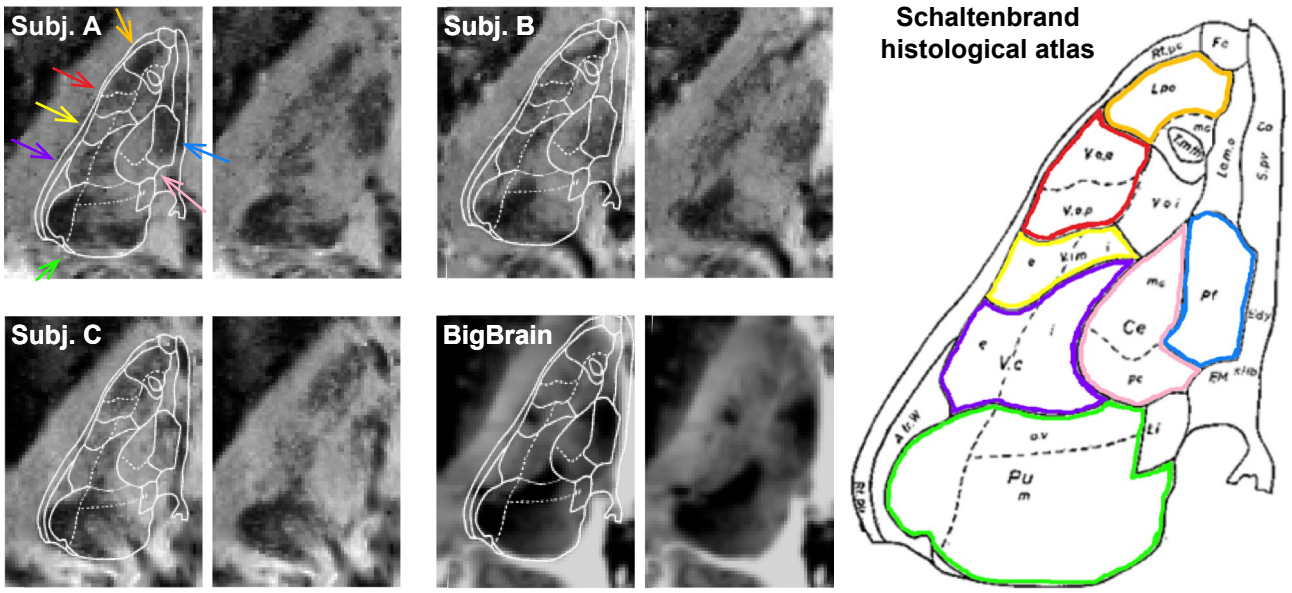

FIGURE 8 Image contrast in the right thalamus of 3 example subjects, in MNI space, for an axial slice positioned at $z = 3.5$ mm, expected to contain multiple thalamic nuclei groups. A reference slice adapted from the Schaltenbrand histological atlas[57] is also shown for the same position ($z = 3.5$ mm). The SWI data are shown with and without an overlay of the atlas contours, delineating the different nuclei groups, for anatomical comparison. The colored arrows indicate the nuclei identified with the same colors on the atlas (right side), comprising the latero-polaris (Lpo), ventro-odalis (Vo), ventral intermediate nucleus (Vim), ventro-caudalus (Vc), pulvinar (Pu), centromedian (Ce) and parafascicular (Pf). The BigBrain reference is also shown in the same position; its contrast is hypo-intense for regions of higher cell body density[58]

4.1 | Motion and field artifact correction

Despite continued efforts to accelerate MRI acquisitions,[61,62] high-resolution 3D scans still typically require several minutes for completion, during which time even very compliant subjects can move by at least some hundreds of micrometers.[63] The data collected in this work appear in line with this description, showing head displacements of 0.12-0.41 mm during the SWI scans (Supporting Information Figure S2). While this indicates a relatively good subject performance, the extent of motion is nevertheless comparable to the in-plane voxel width (0.375 mm). Accordingly, the resulting images were generally of acceptable quality, and would likely be considered of diagnostic value in numerous applications; nonetheless, some of the finer features did exhibit visible blurring and ringing effects in several cases (eg, Figure 3A), effectively compromising the level of specificity originally sought.

In parallel with motion, perturbations of the B_0 field were found averaging at 1.6-4.6 Hz in amplitude, a range that is consistent with previous reports.[26,27,64,65] The field perturbations contained both slow-drift and faster oscillatory patterns, which have been previously observed as well.[64,65] The oscillatory contributions can be clearly attributed to the breathing cycle[64]; the slower contributions could have diverse origins, including other physiological and metabolic sources,[64] but may have been strongly driven by drifts in head position/orientation, as these have been found to generate important perturbations in the measured field at a similar order of magnitude.[66] From these perturbations resulted diverse image artifacts (eg, Figure 3B), also consistent with previous reports.[26,65] The contributions from motion and field perturbations did vary in their relative importance across subjects, likely related to both performance and individual anatomy. Altogether, these observations demonstrate the importance of both motion and field perturbations in high-resolution susceptibility imaging, even in realistic conditions of restricted head motion and natural breathing, thereby supporting, and complementing, previous methodological works.[24-29,40,64,65,67]

The use of integrated navigators allowed substantially mitigating both motion and field artifacts, retrospectively. Despite a relatively good subject performance, this approach still yielded improvements of up to 76% in image quality across the brain. The motion and field correction steps each produced visible, specific improvements in local image features (Figure 3). Across the group, the corrections were found to mitigate the originally observed decreases in image quality with increasing displacement/field deviations (Figure 1), thereby making the resulting images less dependent on the subject performance. Nonetheless, the most affected cases still tended to rank lower than the least affected ones after correction, suggesting room for further improvements. Previous dedicated studies can also provide additional insight on how the FatNav and FatNav + FIDNav approach could potentially perform in regimes of larger motion and field perturbations, which could be relevant for other clinical applications.[33,34,40,68]

In this report, the impact of motion and field perturbations was analyzed not only on the magnitude but also on the phase data, which is of crucial importance to susceptibility-based modalities, such as SWI, phase imaging, quantitative susceptibility mapping (QSM), and susceptibility tensor imaging (STI).[2,64] Like the magnitude, phase images showed decreased quality with increasing displacement/field deviations, across the brain and more particularly at the thalamus (Figure 1). The latter observation is possibly linked to the presence of valuable contrast features in the thalamus for the phase data, which SWI favorably exploits. Compared to the magnitude, the improvements in phase image quality with artifact correction were more moderate, but nevertheless well visible in the data (Figure 3). Interestingly, some of the artifacts that strongly affected the magnitude were not particularly noticeable on the phase (eg, Figure 3B, putamen/globus pallidus), and vice-versa, supporting their distinct profiles of anatomical information, and artifact sensitivity. Beyond SWI, these findings also stress the importance of both motion and field correction for high-resolution susceptibility modalities, including QSM and STI, as previously pointed out by others as well.[64]

4.2 | Vein segmentation and exclusion

The vein detection approach was generally found considerably effective, demonstrating high specificity for features of tubular geometry, while sparing non-venous structures that also appeared hypo-intense, and likely of anatomical relevance (Figure 4B). This is in agreement with previous studies reporting a good performance of this technique on SWI and other MRI modalities.[52-54] Across the range of vessel scales probed by the filter, only a few of the smallest-caliber veins were missed (eg, Figure 4A, red arrows). These occurrences could be in part due to partial volume effects, especially across the slice direction, given the high anisotropy of SWI voxel dimensions. On the other hand, this anisotropy is important for venous contrast,[8,69] and overall, such false negatives were fairly rare, particularly inside the thalamus. Concordantly, the distribution of vein densities in the thalamus estimated from this segmentation was fairly robust across subjects, and consistent with the expected anatomy.[54,60] The group results could be linked to specific, well-defined veins on several of the individual images (eg, Figure 5B), demonstrating the excellent capabilities of high-resolution SWI at 7T for venography, including applications targeting the thalamic veins.

In principle, if necessary for certain targets other than the thalamus, the range of spatial scales covered by the filter could be expanded beyond the limit of 1.2 mm used in this work, and in principle would allow the detection of the larger-caliber vessels that were missed here (Figure 4B).[54] From a technical standpoint, the adopted interpolation approach does not impose any specific requirements on the shape and size of the masked regions, and would remain fully applicable, simply relying on its intrinsic assumptions to fill-in the masked region.[36] However, it is important to keep in mind that, apart from partial volume effects, there is no actual brain tissue in the regions marked as veins. For smaller-caliber vessels, these partial volume effects will have a relatively larger contribution, and the intensities given by interpolation can still provide useful estimates of the local non-venous compartments present in those vein-dominated voxels. When covering larger-caliber vessels, moreover , the information filled-in will be, in this sense, increasingly more "artificial," and should be considered simply as a means to ease visualization and/or subsequent image processing steps. For certain applications, such as intensity-based segmentation/classification, the vein masks could alternatively be used to just exclude those voxels from the analyses, without attributing actual estimates. Nevertheless, overall, at the level of the thalamus, the caliber of vessels actually penetrating the thalamic regions was fairly moderate (Figures 4B and 5B), and the non-venous anatomical features observed with SWI tended to be more spatially extended, and less sharply defined than the veins (Figures 7 and 8); this suggests that the intensities given by interpolation still provide fairly accurate estimates of the non-venous tissue present in the vein-dominated voxels.

4.3 | SWI-based thalamic imaging

As initially hypothesized, variations in the SWI combination parameters created substantial changes on the resulting contrast (Figure 6), and improvements inside the thalamus were observed for parameters considerably beyond those of conventional SWI. This is not wholly unexpected given that the latter was optimized for vein imaging,[7] whereas thalamic nuclei differentiation should depend on considerably different features of tissue composition, microstructure and spatial extent.[2,5] Importantly, because phase effects extend beyond their originating regions, the high-pass filtering parameter σ required particular attention, to avoid introducing misleading non-local features when exploring more permissive filters. This behavior was not found problematic for the range of parameters tested, with the observed features remaining fairly well localized (Figure 6). Nonetheless, it is expected that the observed features will invariably appear larger than the underlying anatomical features, as is already the case for veins in conventional SWI. Likely evidence of this effect can be seen on the observed extent of the RN and STN across slices, when compared to atlas information (Supporting Information Figure S10)—this, however, is unrelated to the phase filtering process, as that was applied in 2D, slice by slice.

In line with insights from previous studies,[13] the diverse anatomical comparisons performed in this work provide compelling evidence for the ability to differentiate several nuclei and nuclei groups within the thalamus with SWI (Figure 7), especially rich in lower intermediate cuts at the level of the Vim nucleus, for instance (Figure 8). The underlying mechanisms by which these tissues may generate the observed contrast remain, however, unclear. Previous works with diffusion-based modalities suggest complex variations in microstructure across the thalamic nuclei,[14,23] and studies on the phase of the MR signal in white matter have shown that it is strongly affected by axonal orientation with respect to the main magnetic field.[70] Cell body density may also play a relevant role, considering the similarities and differences found here between the SWI and BigBrain data (Figures 7 and 8). This issue further relates to the rather empirical nature of SWI, especially for vein-unrelated applications, and may be overcome in the future with more comprehensive studies exploring quantitative modalities such as QSM and STI, at high resolution.

While technically more demanding and less practical to carry out routinely,[2] QSM and STI could prove valuable to clarify the underlying contrast mechanisms, and provide clues to the development of further improved, and more practical new modalities. In the meantime, the results obtained in this work indicate that optimizing the SWI phase-magnitude combination provides an effective way to substantially enhance contrast in the thalamus, which can be fairly easily implemented. Future work could also include attempting this enhancement strategy at lower field strengths, which are currently more widely available in the clinics, but where, to our knowledge, little intra-thalamic contrast can typically be observed.[71]

5 | CONCLUSION

High-resolution susceptibility-weighted modalities at 7T can strongly benefit from motion and breathing artifact corrections. In parallel, optimizing the SWI phase-magnitude combination provides an effective and straightforward way to improve contrast in the thalamus beyond the capabilities of conventional SWI, enhancing features with solid anatomical correspondence to known thalamic nuclei. Vein detection and suppression further improves thalamic visualization. Altogether, these developments substantially improve the capabilities of SWI for non-invasive thalamic nuclei imaging, a challenging task of importance to numerous scientific and clinical applications, including functional neurosurgery.

ACKNOWLEDGMENTS

This work was supported by Centre d'Imagerie BioMédicale (CIBM) of the UNIL, UNIGE, HUG, CHUV, EPFL and the Leenaards and Jeantet Foundations, as well as the Swiss National Science Foundation through Grants 157040 and 205321_153564.

ORCID

João Jorge https://orcid.org/0000-0001-6667-1868
Frédéric Gretsch https://orcid.org/0000-0002-3229-5443

REFERENCES

1. Lee J, Shmueli K, Fukunaga M, et al. Sensitivity of MRI resonance frequency to the orientation of brain tissue microstructure. *Proc Natl Acad Sci USA*. 2010;107:5130–5135.
2. Liu C, Li W, Tong KA, Yeom KW, Kuzminski S. Susceptibility-weighted imaging and quantitative susceptibility mapping in the brain. *J Magn Reson Imaging*. 2015;42:23–41.
3. Edelstein WA, Glover GH, Hardy CJ, Redington RW. The intrinsic signal-to-noise ratio in NMR imaging. *Magn Reson Med*. 1986;3:604–618.
4. Duyn JH. The future of ultra-high field MRI and fMRI for study of the human brain. *NeuroImage*. 2012;62:1241–1248.
5. Duyn JH, van Gelderen P, Li TQ, de Zwart JA, Koretsky AP, Fukunaga M. High-field MRI of brain cortical substructure based on signal phase. *Proc Natl Acad Sci U S A*. 2007;104:11796–11801.
6. Deistung A, Schafer A, Schweser F, Biedermann U, Turner R, Reichenbach JR. Toward in vivo histology: a comparison of quantitative susceptibility mapping (QSM) with magnitude-, phase-, and R2*-imaging at ultra-high magnetic field strength. *NeuroImage*. 2013;65:299–314.
7. Haacke EM, Xu Y, Cheng YC, Reichenbach JR. Susceptibility weighted imaging (SWI). *Magn Reson Med*. 2004;52:612–618.
8. Deistung A, Rauscher A, Sedlacik J, Stadler J, Witoszynskyj S, Reichenbach JR. Susceptibility weighted imaging at ultra high magnetic field strengths: theoretical considerations and experimental results. *Magn Reson Med*. 2008;60:1155–1168.
9. Mittal S, Wu Z, Neelavalli J, Haacke EM. Susceptibility-weighted imaging: technical aspects and clinical applications, part 2. *Am J Neuroradiol*. 2009;30:232–252.
10. Pittau F, Baud MO, Jorge J, et al. MP2RAGE and susceptibility-weighted imaging in lesional epilepsy at 7T. *J Neuroimaging*. 2018;28:365–369.
11. Pitt D, Boster A, Pei W, et al. Imaging cortical lesions in multiple sclerosis with ultra-high-field magnetic resonance imaging. *Arch Neurol*. 2010;67:812–818.
12. De Ciantis A, Barkovich AJ, Cosottini M, et al. Ultra-high-field MR imaging in polymicrogyria and epilepsy. *Am J Neuroradiol*. 2015;36:309–316.
13. Abosch A, Yacoub E, Ugurbil K, Harel N. An assessment of current brain targets for deep brain stimulation surgery with susceptibility-weighted imaging at 7 tesla. *Neurosurgery*. 2010;67:1745-1756; discussion 1756.
14. Behrens TE, Johansen-Berg H, Woolrich MW, et al. Non-invasive mapping of connections between human thalamus and cortex using diffusion imaging. *Nat Neurosci*. 2003;6:750–757.
15. Saalmann YB, Kastner S. Cognitive and perceptual functions of the visual thalamus. *Neuron*. 2011;71:209–223.
16. Byne W, Hazlett EA, Buchsbaum MS, Kemether E. The thalamus and schizophrenia: current status of research. *Acta Neuropathol*. 2009;117:347–368.

17. Louis ED, Ferreira JJ. How common is the most common adult movement disorder? Update on the worldwide prevalence of essential tremor. *Mov Disord*. 2010;25:534–541.
18. Kondziolka D, Ong JG, Lee JY, Moore RY, Flickinger JC, Lunsford LD. Gamma knife thalamotomy for essential tremor. *J Neurosurg*. 2008;108:111–117.
19. Tuleasca C, Bolton TAW, Regis J, et al. Normalization of aberrant pretherapeutic dynamic functional connectivity of extrastriate visual system in patients who underwent thalamotomy with stereotactic radiosurgery for essential tremor: a resting-state functional MRI study. *J Neurosurg*. 2019;1–10.
20. Tuleasca C, Najdenovska E, Regis J, et al. Clinical response to Vim's thalamic stereotactic radiosurgery for essential tremor is associated with distinctive functional connectivity patterns. *Acta Neurochir*. 2018;160:611–624.
21. Tuleasca C, Najdenovska E, Regis J, et al. Pretherapeutic motor thalamus resting-state functional connectivity with visual areas predicts tremor arrest after thalamotomy for essential tremor: tracing the cerebello-thalamo-visuo-motor network. *World Neurosurg*. 2018;117:e438–e449.
22. Elias WJ, Lipsman N, Ondo WG, et al. A randomized trial of focused ultrasound thalamotomy for essential tremor. *New England J Med*. 2016;375:730–739.
23. Najdenovska E, Tuleasca C, Jorge J, et al. Comparison of MRI-based automated segmentation methods and functional neurosurgery targeting with direct visualization of the Ventro-intermediate thalamic nucleus at 7T. *Sci Rep*. 2019;9:1–13.
24. Maclaren J, Armstrong BS, Barrows RT, et al. Measurement and correction of microscopic head motion during magnetic resonance imaging of the brain. *PLoS ONE*. 2012;7:e48088.
25. van Gelderen P, de Zwart JA, Starewicz P, Hinks RS, Duyn JH. Real-time shimming to compensate for respiration-induced B0 fluctuations. *Magn Reson Med*. 2007;57:362–368.
26. Duerst Y, Wilm BJ, Wyss M, et al. Utility of real-time field control in T2*-weighted head MRI at 7T. *Magn Reson Med*. 2016;76:430–439.
27. Jorge J, Gretsch F, Gallichan D, Marques JP. Tracking discrete off-resonance markers with three spokes (trackDOTS) for compensation of head motion and B0 perturbations: accuracy and performance in anatomical imaging. *Magn Reson Med*. 2018;79:160–171.
28. Maclaren J, Herbst M, Speck O, Zaitsev M. Prospective motion correction in brain imaging: a review. *Magn Reson Med*. 2013;69:621–636.
29. Haeberlin M, Kasper L, Barmet C, et al. Real-time motion correction using gradient tones and head-mounted NMR field probes. *Magnetic Reson Med*. 2015;74:647–660.
30. Xiao Y, Zitella LM, Duchin Y, et al. Multimodal 7T imaging of thalamic nuclei for preclinical deep brain stimulation applications. *Front Neurosci*. 2016;10:1–15.
31. Najdenovska E, Tuleasca C, Jorge J, et al. Towards an automated segmentation of the ventrointermediate thalamic nucleus. *6th MICCAI Workshop on Clinical Image-based Procedures*. Quebec City, Canada; 2017.
32. Gallichan D, Marques JP, Gruetter R. Retrospective correction of involuntary microscopic head movement using highly accelerated fat image navigators (3D FatNavs) at 7T. *Magn Reson Med*. 2016;75:1030–1039.
33. Gretsch F, Marques JP, Gallichan D. Investigating the accuracy of FatNav-derived estimates of temporal B0 changes and their application to retrospective correction of high-resolution 3D GRE of the human brain at 7T. *Magn Reson Med*. 2018;80:585–597.
34. Gretsch F, Kober T, Waszak M, Marques JP, Gallichan D. *High Temporal Resolution Retrospective Motion and B0 Correction Using FIDNavs and Segmented FatNavs at 7T*. In Proceedings of the 24th annual ISMRM meeting, Singapore, 2016. Abstract 4251.
35. Frangi AF, Niessen WJ, Vincken KL, Viergever MA. Multiscale vessel enhancement filtering. *Lect Notes Comput Sci*. 1998;1496:130–137.
36. Wang GJ, Garcia D, Liu Y, de Jeu R, Dolman AJ. A three-dimensional gap filling method for large geophysical datasets: application to global satellite soil moisture observations. *Environ Modell Softw*. 2012;30:139–142.
37. Uecker M, Ong F, Tamir JI, et al. *Berkeley Advanced Reconstruction Toolbox*. In Proceedings of the 23rd annual ISMRM meeting, Toronto, Canada, 2015. Abstract 2486.
38. Smith SM, Jenkinson M, Woolrich MW, et al. Advances in functional and structural MR image analysis and implementation as FSL. *NeuroImage*. 2004;23(Suppl 1):S208–S219.
39. Marques JP, Kober T, Krueger G, van der Zwaag W, Van de Moortele PF, Gruetter R. MP2RAGE, a self bias-field corrected sequence for improved segmentation and T1-mapping at high field. *NeuroImage*. 2010;49:1271–1281.
40. Gallichan D, Marques JP. Optimizing the acceleration and resolution of three-dimensional fat image navigators for high-resolution motion correction at 7T. *Magn Reson Med*. 2016;77:547–558.
41. Babayeva M, Kober T, Knowles B, et al. Accuracy and precision of head motion information in multi-channel free induction decay navigators for magnetic resonance imaging. *IEEE Trans Med Imaging*. 2015;34:1879–1889.
42. Bilgic B, Marques JP, Wald LL, Setsompop K. Block coil compression for virtual body coil without phase singularities. In Proceedings of the 4th international workshop on MRI phase contrast & quantitative susceptibility mapping, Graz, Austria, 2016.
43. Uecker M, Lai P, Murphy MJ, et al. ESPIRiT–an eigenvalue approach to autocalibrating parallel MRI: where SENSE meets GRAPPA. *Magn Reson Med*. 2014;71:990–1001.
44. Bilgic B, Ye H, Wald LL, Setsompop K. Simultaneous time interleaved multislice (STIMS) for rapid susceptibility weighted acquisition. *NeuroImage*. 2017;155:577–586.
45. Zhang T, Pauly JM, Vasanawala SS, Lustig M. Coil compression for accelerated imaging with Cartesian sampling. *Magn Reson Med*. 2013;69:571–582.
46. Schofield MA, Zhu Y. Fast phase unwrapping algorithm for interferometric applications. *Opt Lett*. 2003;28:1194–1196.
47. Zhou D, Liu T, Spincemaille P, Wang Y. Background field removal by solving the Laplacian boundary value problem. *NMR Biomed*. 2014;27:312–319.
48. Neelavalli J, Cheng YC, Jiang J, Haacke EM. Removing background phase variations in susceptibility-weighted imaging using a fast, forward-field calculation. *J Magn Reson Imaging*. 2009;29:937–948.
49. McGee KP, Manduca A, Felmlee JP, Riederer SJ, Ehman RL. Image metric-based correction (autocorrection) of motion effects: analysis of image metrics. *J Magn Reson Imaging*. 2000;11:174–181.
50. Loktyushin A, Nickisch H, Pohmann R, Scholkopf B. Blind retrospective motion correction of MR images. *Magn Reson Med*. 2013;70:1608–1618.
51. Smith SM. Fast robust automated brain extraction. *Hum Brain Mapp*. 2002;17:143–155.

52. Koopmans PJ, Barth M, Norris DG. Layer-specific BOLD activation in human V1. *Hum Brain Mapp*. 2010;31:1297–1304.
53. Jorge J, Figueiredo P, Gruetter R, van der Zwaag W. Mapping and characterization of positive and negative BOLD responses to visual stimulation in multiple brain regions at 7T. *Hum Brain Mapp*. 2018;39:2426–2441.
54. Bernier M, Cunnane SC, Whittingstall K. The morphology of the human cerebrovascular system. *Hum Brain Mapp*. 2018;39:4962–4975.
55. Wang Y, Yu Y, Li D, et al. Artery and vein separation using susceptibility-dependent phase in contrast-enhanced MRA. *J Magn Reson Imaging*. 2000;12:661–670.
56. Morel A, Magnin M, Jeanmonod D. Multiarchitectonic and stereotactic atlas of the human thalamus. *J Comp Neurol*. 1997;387:588–630.
57. Schaltenbrand G, Wahren W. *Atlas for stereotaxy of the human brain*. 2nd ed. Thieme; 1977.
58. Amunts K, Lepage C, Borgeat L, et al. BigBrain: an ultrahigh-resolution 3D human brain model. *Science*. 2013;340:1472–1475.
59. Jenkinson M, Bannister P, Brady M, Smith S. Improved optimization for the robust and accurate linear registration and motion correction of brain images. *NeuroImage*. 2002;17:825–841.
60. Giudicelli G, Salamon G. The veins of the thalamus. *Neuroradiology*. 1970;1:92–98.
61. Setsompop K, Feinberg DA, Polimeni JR. Rapid brain MRI acquisition techniques at ultra-high fields. *NMR Biomed*. 2016;29:1198–1221.
62. Liang D, Liu B, Wang J, Ying L. Accelerating SENSE using compressed sensing. *Magn Reson Med*. 2009;62:1574–1584.
63. Reuter M, Tisdall MD, Qureshi A, Buckner RL, van der Kouwe AJW, Fischl B. Head motion during MRI acquisition reduces gray matter volume and thickness estimates. *NeuroImage*. 2015;107:107–115.
64. Wen J, Cross AH, Yablonskiy DA. On the role of physiological fluctuations in quantitative gradient echo MRI: implications for GEPCI, QSM, and SWI. *Magn Reson Med*. 2015;73:195–203.
65. Versluis MJ, Peeters JM, van Rooden S, et al. Origin and reduction of motion and f0 artifacts in high resolution T2*-weighted magnetic resonance imaging: application in Alzheimer's disease patients. *NeuroImage*. 2010;51:1082–1088.
66. Liu J, de Zwart JA, van Gelderen P, Murphy-Boesch J, Duyn JH. Effect of head motion on MRI B0 field distribution. *Magn Reson Med*. 2018;80:2538–2548.
67. Mattern H, Sciarra A, Lusebrink F, Acosta-Cabronero J, Speck O. Prospective motion correction improves high-resolution quantitative susceptibility mapping at 7T. *Magn Reson Med*. 2019;81:1605–1619.
68. Gretsch F, Mattern H, Gallichan D, Speck O. Fat navigators and Moire phase tracking comparison for motion estimation and retrospective correction. *Magn Reson Med*. 2020;83:83–93.
69. Xu Y, Haacke EM. The role of voxel aspect ratio in determining apparent vascular phase behavior in susceptibility weighted imaging. *Magn Reson Imaging*. 2006;24:155–160.
70. Wharton S, Bowtell R. Effects of white matter microstructure on phase and susceptibility maps. *Magn Reson Med*. 2015;73:1258–1269.
71. Ladd ME, Bachert P, Meyerspeer M, et al. Pros and cons of ultra-high-field MRI/MRS for human application. *Prog Nucl Magn Reson Spectrosc*. 2018;109:1–50.

SUPPORTING INFORMATION

Additional Supporting Information may be found online in the Supporting Information section.

FIGURE S1 Sequence kernel diagram of the 3D GRE acquisition employed in this work for SWI. The host sequence parts are shown in blue (without flow compensation gradients, for clarity), and the integrated navigators in green. An FIDNav is placed after the host RF excitation, and two double-echo FatNav k-space line acquisitions after the host readout. In practice, the physical encoding directions of the FatNavs were different from those of the host. This kernel was repeated until the desired k-space data of the GRE was fully acquired (ie, the dashed gradients change over the acquisition)

FIGURE S2 Head motion and field fluctuations exhibited by individual subjects during the 11-min acquisition time of the high-resolution GRE (SWI) data, as estimated from the navigator measurements. Six example subjects are shown, selected so as to uniformly cover the range of head motion amplitudes (RMS) observed in the full group. The head displacement at each timepoint was estimated as the norm of the displacement of each voxel in the brain relative to its position at the time of acquisition of the center of k-space (which occurred just before the 4-min mark), averaged across all brain voxels. The timecourses are colored according to the RMS of each subject's displacement across the acquisition time, from blue (lowest displacement RMS) to red (largest displacement RMS). The in-plane voxel resolution of the acquisition (0.375 mm) is marked by a traced black line, for reference. The field deviation at each timepoint was calculated as the absolute field shift relative to B_0 in each voxel (based on the 1st order distribution estimated from the FatNavs), averaged across all brain voxels. Each timecourse is presented in the same color as the corresponding motion plot

FIGURE S3 Global improvements in GRE magnitude and phase data achieved with motion and field artifact correction, in a full brain slice for two example subjects (the same subjects as in Figure 3). Subject A exhibited a relatively larger incidence of motion (0.28 mm displacement RMS) than field perturbations (1.97 Hz deviation RMS); subject B exhibited the opposite (0.13 mm displacement, 3.66 Hz deviation). The gradient squared estimates for each magnitude and phase image are indicated on the respective top right corner

FIGURE S4 Local improvements in GRE magnitude and phase data achieved with motion and field artifact correction, expressed as difference maps, in two example subjects (same subjects and regions as in Figure 3). Subject A exhibited a relatively larger incidence of motion (0.28 mm displacement RMS) than field perturbations (1.97 Hz deviation RMS); subject B exhibited the opposite (0.13 mm displacement, 3.66 Hz deviation). Both panels of each row are shown in the same gray scale, to allow comparisons across the two

correction steps; the gray scales are normalized to the strongest difference in each row. The colored arrows and circles highlight the same regions as in Figure 3

FIGURE S5 Improvements in GRE magnitude and phase data achieved with motion and field artifact correction, in an example subject. This subject exhibited a relatively low incidence of motion (0.12 mm average displacement) and moderate field perturbations (3.07 Hz average deviation), resulting in high image quality, even without corrections, and in negligible changes after correction. The gradient squared estimates for each magnitude and phase image are indicated on the respective top right corner. Also shown are the difference maps across the different correction steps. Both panels of each row are shown in the same gray scale, to allow comparisons across the two correction steps; the gray scales are normalized to the strongest difference in each row

FIGURE S6 Vein detection and interpolation in the SWI data (conventional contrast) of an example subject, across a full brain slice. The vesselness filter output is shown overlaid on the SWI data (right side), thresholded with the same cutoff applied to create the vein masks. This example further shows the advantages of the filter over a simple intensity thresholding approach, as it detected the vast majority of vessels present in the image, while preserving other hypointense regions such as the putamen and globus pallidus

FIGURE S7 Performance of vessel enhancement filtering when applied in 2D (slice by slice) vs. a full 3D form. The filter outputs are shown overlaid on a series of three consecutive slices of a representative example, with both cases having been tuned independently to ensure optimal performance. Overall, the 3D filter produced patterns that were consistently coarser and blurrier than in 2D, and showed higher occurrences of both false negatives (eg, green circle) and false positives (eg, blue circle), even with a dedicated optimization. It is strongly likely that this difference in performance may be related to the substantial anisotropy of the voxel dimensions, with the 3D filter generating maps at a compromise between the high in-plane resolution (0.375 mm) and the relatively coarser slice resolution (1 mm). The only cases observed where the 3D form outperformed 2D were in some larger-caliber vessels running perpendicularly to the slice plane (eg, black circle), which the 2D form could not identify, most likely because their in-plane shape is close to circular, not tubular. Given its overall superiority, especially for thalamic imaging purposes, the 2D form was therefore preferred

FIGURE S8 Correspondence between the vendor-supplied, online SWI reconstruction in our system, and the SWI contrasts yielded by the offline reconstruction pipeline employed in this work (described in Sections 2.2 and 2.5), for an example subject. A, Normalized mean absolute error across voxels (nMAE, shown as a % of the mean image intensity) between the online SWI and images obtained with different combinations of Gaussian phase filtering FWHM (σ) and number of mask multiplications (m). The outcome closest to the online reconstruction (lowest nMAE) was found for a combination of $\sigma = 4$ mm, $m = 4$. B, Visual comparison between the online reconstruction and the closest selected case (referred to as "conventional" in the main text), in an illustrative region

FIGURE S9 Image contrast in the thalamus of two example subjects (A and B) obtained with different imaging modalities, co-registered to the SWI native space: T_1-weighted contrast from the MP2RAGE acquisition (1st column); SWI with close-to-conventional contrast, that is, the closest output of our approach ($\sigma = 4$ mm, $m = 4$) to the scanner online reconstruction (2nd column; marked with a * to highlight its difference from the originally proposed approach[7]); and SWI with enhanced contrast ($\sigma = 7$ mm, $m = 10$; 3rd column). Reference information from the Morel atlas (4th column) and BigBrain (5th column) are shown for anatomical comparison; the colors of the Morel atlas are attributed randomly, simply to differentiate its sub-regions; the contrast in BigBrain is hypo-intense for regions of higher cell body density.[58] Three slices are shown, ascending through the thalamus from the bottom to the top row; the numbers on the top-left indicate the slices selected from the native SWI space. Of note, the middle slice ($s = 30$ or $s = 28$ for A or B respectively) is approximately the most caudal slice passing by the MD nucleus; for this reason, and most likely due to individual anatomical variability, the MD no longer appears in BigBrain for this slice, while it is still present in the SWI data

FIGURE S10 Image contrast in the thalamus of an example subject obtained with different imaging modalities, co-registered to the SWI native space: T_1-weighted contrast from the MP2RAGE acquisition (1st column); SWI with close-to-conventional contrast, that is, the closest output of our approach ($\sigma = 4$ mm, $m = 4$) to the scanner online reconstruction (2nd column; marked with a * to highlight its difference from the originally proposed approach[7]); and SWI with enhanced contrast ($\sigma = 7$ mm, $m = 10$; 3rd column). Reference information from the Morel atlas (4th column) and BigBrain (5th column) are shown for anatomical comparison; the colors of the Morel atlas are attributed randomly, simply to differentiate its sub-regions; the contrast in BigBrain is hypo-intense for regions of higher cell body density.[58] The labels shown near the Morel atlas indicate the sub-thalamic (STN), and red (RN) nuclei. Twenty-two contiguous slices are shown in two columns each, ascending through most of the thalamus; the numbers on the top-left indicate the slices selected from the native SWI space

How to cite this article: Jorge J, Gretsch F, Najdenovska E, et al. Improved susceptibility-weighted imaging for high contrast and resolution thalamic nuclei mapping at 7T. *Magn Reson Med*. 2020;84:1218–1234. https://doi.org/10.1002/mrm.28197